Phys Chem Minerals (2010) 37:103–117
DOI 10.1007/s00269-009-0315-1

ORIGINAL PAPER

Visualization-based analysis of structural and dynamical properties of simulated hydrous silicate melt

Bijaya B. Karki · Dipesh Bhattarai · Mainak Mookherjee · Lars Stixrude

Received: 10 November 2008 / Accepted: 14 May 2009 / Published online: 13 June 2009

Abstract We have explored first-principles molecular dynamics simulation data for hydrous $MgSiO_3$ liquid (with 10 wt% water) to gain insight into its structural and dynamical behavior as a function of pressure (0–150 GPa) and temperature (2,000–6,000 K). By visualizing/analyzing a number of parameters associated with short- and mid-range orders, we have shown that the melt structure changes substantially on compression. The speciation of the water component at low pressures is dominated by the isolated structures (with over 90% hydrogen participated) consisting of hydroxyls, water molecules, O–H–O bridging and four-atom (O–H–O–H and H–O–H–O) groups, where every oxygen atom may be a part of polyhedron or free (i.e., bound to only magnesium atom). Hydroxyls favor polyhedral sites over magnesium sites whereas molecular water is almost entirely bound to magnesium sites, and also interpolyhedral bridging (Si–O–H–O–Si) dominates other types of bridging. Water content is shown to enhance and suppress, respectively, the proportions of hydroxyls and molecular water. As compression increases, these isolated structures increasingly combine with each other to form extended structures involving a total of five or more O and H atoms and also containing threefold coordination species, which together consume over 80% hydrogen at the highest compression studied. Our results show that water lowers the mean coordination numbers of different types including all cation–anion environments. The hydrous melt tends to be more tetrahedrally coordinated but with the Si–Si network being more disrupted compared to the anhydrous melt. Protons increase the content of non-bridging oxygen and decrease the contents of bridging oxygen as well as oxygen triclusters (present at pressures above 10 GPa). The calculated self-diffusion coefficients of all atomic species are enhanced in the presence of water compared to those of the anhydrous melt. This is consistent with the prediction that water depolymerizes the melt structure at all pressures. Our analysis also suggests that proton diffusion involves two processes—the transfer of H atoms (requiring the rupture and formation of O–H bonds) and the motion of hydroxyls as hydrogen carriers (requiring the rupture and formation of Si–O and/or Mg–O bonds). Both the processes are operative at low compression whereas only the first process is operative at high compression.

Keywords Silicate melt · Hydrous phase · Structure · Diffusion · First-principles simulation · Visualization · High pressure

Electronic supplementary material The online version of this article (doi:10.1007/s00269-009-0315-1) contains supplementary material, which is available to authorized users.

B. B. Karki (✉) · D. Bhattarai
Department of Computer Science,
Louisiana State University,
Baton Rouge, LA 70803, USA
e-mail: karki@csc.lsu.edu

B. B. Karki
Department of Geology and Geophysics,
Louisiana State University,
Baton Rouge, LA 70803, USA

M. Mookherjee
Bayerisches Geoinstitut, Universität Bayreuth,
Bayreuth 95440, Germany

L. Stixrude
Department of Earth Sciences,
University College London,
London WC1E 6BT, UK

Introduction

A detailed knowledge of structural and dynamical properties of silicate liquids is crucial for our understanding of the generation and transport mechanisms of magmas. Melts in the Earth's interior are likely to be hydrous (e.g., Tyburczy et al. 1991; Revenaugh and Sipkin 1994; Bercovici and Karato 2003; Sakamaki et al. 2006). Water being perhaps the most abundant volatile component contributes to bubble growth and buoyancy of magmas, facilitating the volcanic eruption process. Water is also a strongly incompatible component that has a dramatic influence on melt structure (Closmann and Williams 1995), solidus temperature and melt composition (Inoue 1994; Yamada et al. 2004), density (Ochs and Lange 1999; Matsukage et al. 2005), diffusivity (Watson 1981; Tinker et al. 2003; Zhang et al. 2007) and viscosity (Lange 1994). The speciation is known to change as a function of total water content from dominantly hydroxyls at low water contents, to dominantly water molecules at higher water contents (Stolper 1982). Whether water dissolves as hydroxyls or molecular water or in some other forms impact the degree of polymerization, which, in turn, controls the transport properties—the less the structure is polymerized the higher the diffusivity (the lower viscosity) (Whittington et al. 2000; Tinker et al. 2003; Giordano et al. 2004). The solubility of water increases rapidly with increasing pressure (Shen and Keppler 1997) and may be unlimited over most mantle pressure–temperature conditions (Mookherjee et al. 2008). Experimental information of melt structure is mostly based on the study of glasses (e.g., Shen and Keppler 1995; Closmann and Williams 1995; Zhang 1999; Yamada et al. 2007; Lee et al. 2008).

In recent years, sophisticated computational approaches based on principles of quantum mechanics have taken on an increased importance in the study of non-crystalline materials including silicate liquids (e.g., Pohlmann et al. 2004; Stixrude and Karki 2005; Wan et al. 2007; Mookherjee et al. 2008). Such first-principles simulations can help us to answer several fundamental questions related to the physical changes that occur in the silicate melt due to water. What are the fundamental forms of water speciation and how do their abundances vary with pressure and temperature? To what extent do the protons behave like other network modifier cations (such as Mg, Ca and Na) in disrupting the tetrahedral silicate network? How is the content of non-bridging oxygen (NBO) affected by the presence of water? How do the effects of water on polymerization vary with pressure? For instance, how does NBO transform into bridging oxygen (BO) as the liquid is compressed? These answers are expected to improve our knowledge of density, thermodynamic properties and transport properties of hydrous silicate melt and their variations with pressure.

In our continuing first-principles investigation of silicate melts (e.g., Stixrude and Karki 2005; Karki et al. 2007; de Koker et al. 2008), we have recently studied a hydrous $MgSiO_3$ liquid with 10 wt% water at high pressure (Mookherjee et al. 2008). In this paper, we report a detailed analysis of the simulated results on the structural and dynamical behavior of hydrous $MgSiO_3$ melt. We examine in detail the radial distribution functions (RDFs) and coordination environments considering all atomic species. This allows us to identify and quantify water speciation, and also estimate the concentrations of NBO ions, oxygen triclusters and over-coordinated cations. Using relatively long runs, we calculate the self-diffusion coefficients of all atomic species and study the influence of water on transport properties through comparisons between hydrous and anhydrous melts. We also explore the hydrogen diffusion mechanisms.

Methodology

First-principles molecular dynamics method (VASP—Vienna ab-initio simulation package) (Kresse and Furthmuller 1996) was used to simulate the liquid systems within the finite temperature formulation of density functional theory (Mermin 1965; Wentzcovitch et al. 1992). The local density approximation (LDA, Ceperley and Alder 1980) was used primarily with select comparisons to results with the generalized gradient approximation (GGA, Wang and Perdew 1991). We show that GGA produces nearly identical melt structures as LDA at the same volume. Ultrasoft pseudopotentials (Kresse and Hafner 1994) were used with a plane wave cutoff of 400 eV and gamma point sampling. Time steps of 0.5 and 1 fs were used for hydrous and anhydrous phases, respectively. Our simulations were based on the canonical (*NVT*) ensemble in which the number of atoms in the periodically repeated unit cell (*N*), the volume (*V*) and the temperature (*T*) are fixed.

The nature of the canonical ensemble, for which volume is the independent variable, has considerable analytical advantages. We find that liquid structure is primarily a function of volume, rather than pressure, and that variations in temperature at constant volume leave mean coordination numbers virtually unchanged. We express the volume as V/V_X, where $V_X = 1{,}033.54$ Å^3 is equal, for the number of atoms in our simulation cell, to the experimental volume of enstatite liquid at the ambient melting point (38.9 cm^3/mol) (Lange and Carmichael 1987). We find that expressing the volume in this way provides an immediate measure of the amount of compression involved and we explore compression from $V/V_X = 1.0$ to $V/V_X = 0.45$ covering wide ranges of pressure (0–150 GPa) and temperature (2,000–6,000 K) (see Supplementary Table 1). For the hydrous systems, we retain the same reference

volume to facilitate comparison to the anhydrous system (Stixrude and Karki 2005). We have chosen the number of atoms in our simulation cell such that V_X is equal to the volume measured experimentally at ambient pressure (Ochs and Lange 1999): 12 $MgSiO_3$ units and 8 H_2O molecules for 10 wt% water (84 atoms total), and 14 $MgSiO_3$ and 4 H_2O for 5 wt% water (82 atoms total). The initial structure at each volume was first melted at 6,000 K, and then cooled isochorically to 4,000 K and then to 3,000 K. At V_X it was further cooled down to 2,500 K and then finally to 2,000 K. We extend the previous runs (Stixrude and Karki 2005; Mookherjee et al. 2008) to ensure that the diffusive regime for all atomic species is reached and well sampled. We confirm that the system at each V–T condition simulated is in the liquid state by examining the RDFs and mean-square displacements. The total durations at V_X are 8, 12, 24, 36 and 90 ps for 6,000, 4,000, 3,000, 2,500 and 2,000 K, respectively. Relatively longer runs were performed at higher compression, e.g., 150 ps at 3,000 K and 0.5 V_X. Previous MD studies have suggested that the effects of finite size, particularly, on dynamical properties can be substantial for highly polymerized liquids like silica (Rustad et al. 1990; Tsuneyuki and Matsui 1995; Zhang et al. 2004). Our tests show that the effects are not significant for the sizes of the order of 100 atoms used in the case of silicate liquids.

Corrections to the pressure were included as in our previous studies (Stixrude and Karki 2005; Mookherjee et al. 2008; de Koker et al. 2008). We report the pressure as

$$P(V) = P_{\mathrm{MD}}(V) + P_{\mathrm{Pulay}}(V) + P_{\mathrm{Emp}}(V). \quad (1)$$

Here, P_{MD} is the pressure computed in our simulations. The Pulay correction is

$$P_{\mathrm{Pulay}}(V) = P_{\mathrm{S}}(V; E_{\mathrm{cut}} = 600\,\mathrm{eV}) - P_{\mathrm{S}}(V; E_{\mathrm{cut}} = 400\,\mathrm{eV}), \quad (2)$$

where P_{S} is the static pressure of crystalline enstatite computed with a higher cutoff of 600 eV to yield fully converged results. We find that P_{Pulay} increases monotonically from 2.2 to 5.8 GPa over the compression regime studied. The empirical correction accounts for the well known and systematic over-binding of LDA. Its value was computed as

$$P_{\mathrm{emp}} = -P_{\mathrm{S}}(V_{\mathrm{exp}}; E_{\mathrm{cut}} = 600\,\mathrm{eV}), \quad (3)$$

where V_{exp} is the experimental zero-pressure volume of enstatite at static conditions computed via the thermodynamic model of Stixrude and Lithgow-Bertelloni (2005). Its value is 1.9 GPa for enstatite, and similar for perovskite. Assuming that these corrections are insensitive to the addition of water, we apply the same corrections to our hydrous systems, finding excellent agreement with experimental measurements of the zero-pressure volume of enstatite liquid and with the partial molar volume of water in silicate liquids at zero-pressure.

The simulations consisting of several thousands of steps per run produce massive datasets for atomic configurations. The space-time multiresolution visualization system (Bhattarai and Karki 2009) was used for gaining insight into important information contained in the simulations. The structural analysis starts with the computation of the RDFs defined as $g_{\alpha\beta}(r)$ for atomic pair of species α and β:

$$g_{\alpha\beta}(r) = \frac{1}{4\pi\rho_\beta r^2}\left[\frac{\mathrm{d}N_\beta(r)}{\mathrm{d}r}\right], \quad (4)$$

where ρ_β is the number density of species β and N_β is the number of species β within a sphere of radius r around a selected atom of type α. The mean bond length

$$\bar{r}_{\alpha\beta} = \frac{\int_0^{r_{\mathrm{min}}^{\alpha\beta}} r g_{\alpha\beta}(r)\mathrm{d}r}{\int_0^{r_{\mathrm{min}}^{\alpha\beta}} g_{\alpha\beta}(r)\mathrm{d}r}, \quad (5)$$

where $r_{\mathrm{min}}^{\alpha\beta}$ is the distance to the first minimum in $g_{\alpha\beta}$, tends to be somewhat larger than the position of the first maximum in $g_{\alpha\beta}$ because the peak is asymmetric. Atomic coordination, which characterizes the local structure, is calculated for a given species α with respect to another species β using

$$C_{\alpha\beta} = 4\pi\rho_\beta \int_0^{r_{\mathrm{min}}^{\alpha\beta}} r^2 g_{\alpha\beta}(r)\mathrm{d}r \quad (6)$$

Both the RDF and mean coordination have limitations as being isotropic so it is important to supplement interpretation of these functions with other structural information by exploring individual snapshots. For the purpose, we calculate the coordination species on per atom basis (ith atom of species α) and as a function of time:

$$C_{\alpha\beta}^i(t) = \left|\left\{1 \le j \le N_\beta : \mathrm{d}(i,j) \le r_{\mathrm{min}}^{\alpha\beta}\right\}\right| \quad \text{for } i = 1,\ldots,N_a, \quad (7)$$

where N_α and N_β are the numbers of atoms of species α and β, respectively, in the system. See Supplementary Figs. 1 and 2 for visualization of the RDF and coordination data. We compute the self-diffusion coefficient as

$$D = \lim_{t\to\infty} \frac{\left\langle [r(t)]^2 \right\rangle}{6t}, \quad \text{where } \left\langle [r(t)]^2 \right\rangle = \frac{1}{N}\sum_{i=1}^{N} |r_i(t+t_0) - r_i(t_0)|^2 \quad (8)$$

is the mean-square displacement (see Supplementary Fig. 3 for MSD plots). The positions of the ith atom at time origin t_0 and then after time t are $r_i(t_0)$ and $r_i(t+t_0)$, respectively.

Structural properties: results and discussion

Radial distribution functions

The calculated partial RDFs vary remarkably in their shapes between different atomic pair types (Figs. 1, 2 and Supplementary Fig. 1). Features common to all functions include the appearance of an initial peak, and a decrease in the magnitude of the fluctuations with increasing distance, approaching unity at the largest distances. These features reflect, respectively, the short-range order and long-range disorder characteristics of the liquid state. The partial RDFs also reflect the dominant role of ionic interactions and charge ordering. Cation–anion functions, namely $g_{SiO}(r)$, $g_{HO}(r)$ and $g_{MgO}(r)$, show the largest amplitudes in their first peaks, and also well-defined minima and broader second peaks (Fig. 1 and Supplementary Table 2). The Si–O RDF is best structured exhibiting the tallest and sharpest peaks among all functions and the value at the minimum after the first peak is almost 0. Other functions show relatively broader and shorter first peak and, in many cases the minimum and the second peak are poorly defined. Also, the peaks are located at relatively larger distances.

Our results for the hydrous melt show that water does not change the shapes of cation–anion RDFs substantially (Fig. 1). Addition of water tends to weaken and broaden the first peaks in the other RDFs including Si–Si, consistent with experiments (Yamada et al. 2007). This is caused by the tendency of water to break Si–O–Si bridges, depolymerizing the melt structure and reducing medium-range order. With increasing temperature, the degree of order decreases, peaks become shorter, wider and less symmetric and the values at the minima increase. On compression, the first peak in the Si–O RDF gradually decreases in the height; both the peak and minimum positions affected, and a new peak rather appears at much shorter distance than the original second peak. In the case of MgO RDF, the heights of the first and second peaks decrease initially and then increase on compression with their positions as well as the minimum position shifting to smaller distances. Following small initial changes, the shape of the O–O RDF changes qualitatively at high compression with a shoulder appearing before the second peak; a feature that has been seen in simulations based on classical potentials (Martin et al. 2009).

Our results compare favorably with experiment. The experimental Si–O peak positions ($\sim$1.64 to $\sim$1.7 Å) at low pressures (Yamada et al. 2007) are comparable to our calculated peak positions and are systematically smaller than our calculated average interatomic distances (peak position

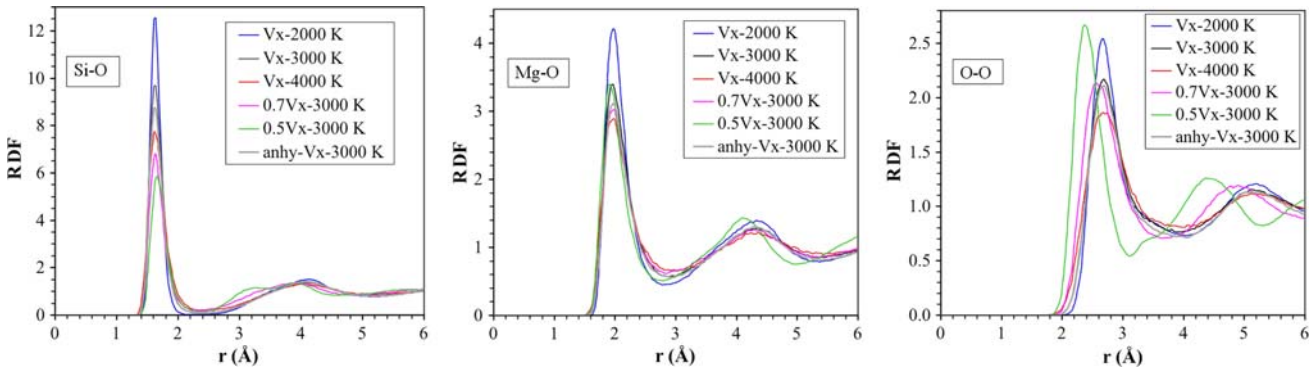

Fig. 1 Calculated Si–O, Mg–O and O–O radial distribution functions of hydrous and anhydrous melts at different conditions

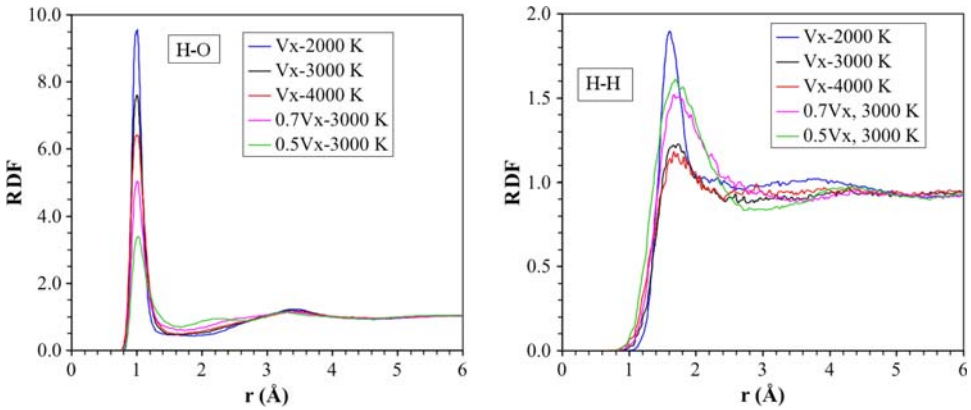

Fig. 2 Calculated H–O and H–H radial distribution functions of hydrous melt at different conditions

of 1.625 Å and average distance of 1.671 Å at V_X and 3,000 K, 2.3 GPa). Also, the experimental Mg–O peak distance of ~2.1 Å lies between the calculated peak position and calculated average distance (peak position of 1.965 Å and average distance of 2.134 Å at V_X and 3,000 K, 2.3 GPa). The discrepancy may be due to limited experimental resolution of the peak asymmetry (Waseda and Toguri 1990; Funamori et al. 2004; Yamada et al. 2007), which is less serious for the much narrower Si–O peak.

The H–O RDF closely resembles the shape of the other cation–anion functions. It shows a sharp first peak (Fig. 2). The only effect of isochoric heating is to reduce the amplitude of the peaks without affecting other features significantly. On compression, the first peak gets increasingly shorter and a new peak appears at a much shorter distance than the original second peak. The amplitude of the first peak in g_{HO} is less than that of g_{SiO}, reflecting the variety of hydrogen species present in the melt. A weak second peak in g_{HO} at 3.375 Å lies at larger H–O separation than that expected for canonical hydrogen bonding and reflects instead the distribution of H species in a dominantly silicate framework. The other H RDFs, $g_{SiH}(r)$, $g_{MgH}(r)$ and g_{HH} suggest that bonding of H to atoms other than O can be excluded. The position of the first peak in $g_{HH}(r)$ is similar to the H–H separation in the free water molecule (Fig. 2). There is no evidence of a tendency toward phase separation as has been found in water, which

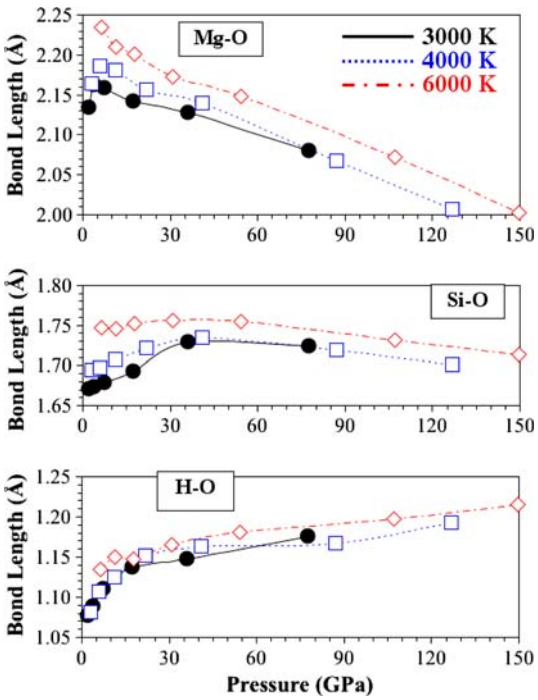

Fig. 3 Average distances as a function of pressure at 3,000 K (*circles*), 4,000 K (*squares*) and 6,000 K (*diamonds*). Note that these distances are larger than the corresponding first peak distances due the asymmetry of the RDF peak and a non-zero value at the minimum

dissociates under certain conditions to H_2 and O_2 molecules (Mao et al. 2006).

The variation on compression of bond lengths (Eq. 5) in the liquid differs markedly from that in crystalline phases (Fig. 3). Whereas in crystals bond lengths almost universally shorten on compression, this is not seen in silicate liquids. Remarkably, all three cation–anionic distances increase initially on compression. This is caused by an increase in coordination number on compression. The predicted small change in the Si–O bond length is consistent with the experimental observations (Yamada et al. 2007). On further compression, the H–O distance keeps on increasing whereas the Mg–O length starts to decrease soon (after 5 GPa) and the Si–O length starts to decease much later (beyond 30 GPa). The evolution of the breadth of the first peak in g_{SiO} on compression shows that polyhedra in the liquid are more irregular than those in crystals and that they become more distorted on compression.

Mean coordination environments

Compression has a profound influence on the mean coordination numbers with their values in most cases monotonically increasing with increasing pressure (Fig. 4 and Supplementary Table 3). In contrast, the effects of increasing temperature at constant volume are small. The Si–O and Mg–O coordination numbers increase gradually from ~4 and ~5, respectively, at low compression to ~6 and ~8, respectively, at the highest compression (Fig. 4, left). A similar pressure-induced increase of Si–O coordination was found experimentally in silicate glasses and melts (Williams and Jeanloz 1988), although in the case of the glass, the coordination change takes places at higher pressures and occurs more suddenly. Whereas in the glass fourfold coordination apparently survives for a substantial pressure interval, in the liquid the coordination change occurs gradually from the lowest pressure, and the mean Si–O coordination number increases nearly linearly with compression. In the hydrous melt, both coordination numbers tend to be smaller than those in the anhydrous melt at the same volume. The difference in Mg–O coordination between two phases can be attributed to the presence of Mg-bound hydroxyls and water groups, which are more prevalent at low pressures. Smaller O–Si coordination shows that water disrupts the inter-polyhedral linkages, which is also manifested in the relatively low hydrous Si–Si coordination (Fig. 4, center) (Mookherjee et al. 2008). Our prediction of depolymerization in the presence of water is consistent with experimental observations (Yamada et al. 2007). Other coordination environments follow the similar trend that their hydrous numbers are smaller than their anhydrous counterparts. This can be rationalized with the view that H atoms in the

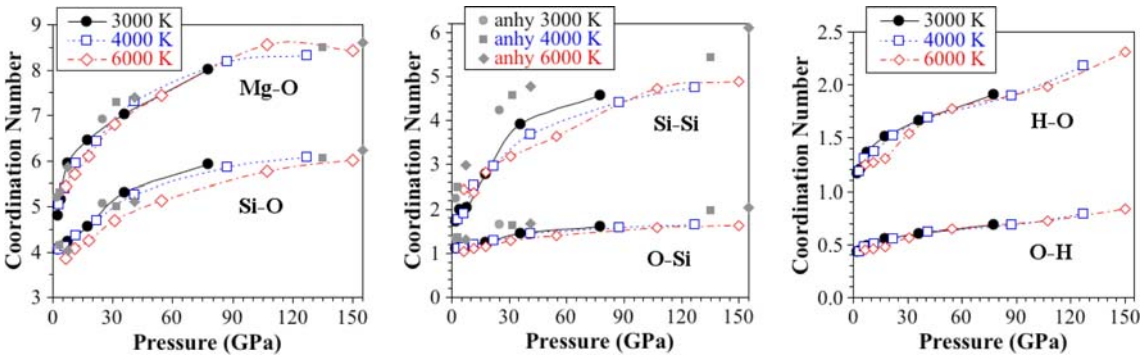

Fig. 4 Mean coordination numbers as a function of pressure at 3,000 K (*solid circles*), 4,000 K (*open squares*) and 6,000 K (*open diamonds*) for six coordination (Mg–O, Si–O, Si–Si, O–Si, H–O and O–H) environments in the hydrous melt. Results for anhydrous phase are shown by *grey solid symbols*

melt are present at the expenses of Mg and Si atoms, and a significant proportion of O atoms are thus engaged in hydrogen bonding.

The mean H–O coordination also increases with compression (Fig. 4, right). The variation is from ~1.2 at low pressure to above 2 at high pressure. The low pressure value is similar to that expected of entirely molecular speciation as isolated hydroxyls or water molecules, consistent with experiment (Stolper 1982). The high pressure value is similar to that in the high-pressure form of water (Goldman et al. 2005), and ice (ice X) (Goncharov et al. 1999) in which the structure is a complete three-dimensional network of nearly symmetric hydrogen bonds. Like other anion–cation coordination, the mean O–H coordination gradually increases from ~0.4 to ~0.8 over the compression range studied. Values lower than the unity means that a significant proportion of oxygen atoms in the liquid do not participate in hydrogen bonding.

Si and O coordination species

The gradual increase in Si–O coordination on compression is facilitated by gradual changes in the concentrations of various coordination species (denoted by ${}_ZC_{\mathrm{SiO}}$, where Z represents the coordination number), of which a mixture is presented at each volume, temperature condition. At low pressure fourfold coordination (${}_4C_{\mathrm{SiO}}$) dominates with noticeable contributions from three- and fivefold coordination (Table 1). On isochoric cooling at low compression, the mean Si–O coordination number remains nearly 4 while the proportion of non-tetrahedral defects decreases, consistent with experimental observation that they are essentially absent in the nearly perfectly tetrahedral room temperature glass. Fivefold coordinated defects are slightly more abundant in the anhydrous phase at the expenses of the four- and threefold coordination, compared to the hydrous phase (Table 1).

Table 1 Abundances of various Si–O and O–Si coordination species (denoted as ${}_ZC_{\mathrm{SiO}}$ and ${}_ZC_{\mathrm{OSi}}$, respectively, where Z represents coordination number) for the hydrous melt and anhydrous melt (*anhy*) at V_X

	${}_2C_{\mathrm{SiO}}$	${}_3C_{\mathrm{SiO}}$	${}_4C_{\mathrm{SiO}}$	${}_5C_{\mathrm{SiO}}$	${}_6C_{\mathrm{SiO}}$
2,000 K	0.00	0.07	97.91	2.01	0.00
2,500 K	0.00	0.67	95.98	3.29	0.06
Anhy	0.00	0.48	92.83	6.49	0.20
3,000 K	0.00	1.70	90.19	7.77	0.34
*	0.00	1.43	90.01	8.41	0.15
Anhy	0.00	1.37	87.49	10.92	0.22
4,000 K	0.35	8.94	76.42	13.85	0.44
Anhy	0.25	5.94	73.60	19.20	1.01
	${}_0C_{\mathrm{OSi}}$	${}_1C_{\mathrm{OSi}}$	${}_2C_{\mathrm{OSi}}$	${}_3C_{\mathrm{OSi}}$	${}_4C_{\mathrm{Osi}}$
2,000 K	12.15	66.12	21.69	0.04	0.00
2,500 K	11.66	66.87	21.43	0.04	0.00
Anhy	2.30	63.01	34.38	0.31	0.00
3,000 K	12.47	64.40	22.89	0.25	0.00
*	8.33	59.81	31.49	0.38	0.00
Anhy	2.49	61.75	35.16	0.59	0.00
4,000 K	13.79	62.71	22.75	0.75	0.00
Anhy	4.53	57.28	36.48	1.71	0.02

Results for low water content (5 wt%) melt are marked *

On compression, contributions from five- and sixfold coordination increase whereas those from three- and fourfold coordination decrease (Fig. 5, left). The preponderance of ${}_5C_{\mathrm{SiO}}$ species at mid compression (around 30 GPa at 3,000 K, and at higher pressures at higher temperatures) also predicted to occur in other silicate liquids (Angell et al. 1982; Karki et al. 2007) demonstrates that liquid structure is not merely a disordered version of the structure of the crystalline polymorphs, ${}_5C_{\mathrm{SiO}}$ being extremely rare in crystalline silicates. Fivefold coordination has been suggested as a transition state that enhances diffusion

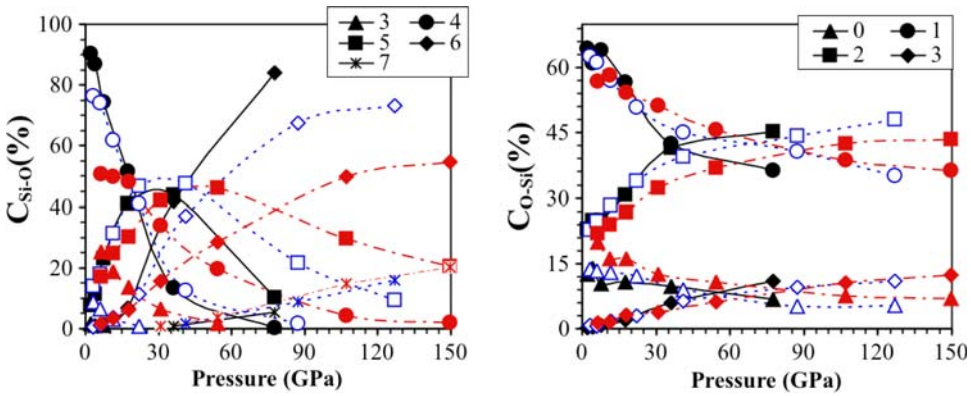

Fig. 5 Abundances of different Si–O and O–Si coordination species as a function of pressure at 3,000 K (*black solid lines* and *black symbols*), 4,000 K (*blue dotted lines* and *blue symbols*) and 6,000 K (*red dashed-dotted lines* and *red symbols*) for the hydrous melt

through the exchange of oxygen. At high compression, sixfold coordination dominates and its contribution decreases with increasing temperature with the appearance of ${}_7C_{SiO}$ and ${}_8C_{SiO}$ species.

Similarly, the relative abundances of different O–Si coordination species change upon compression (Fig. 5, right). The anhydrous liquid has 22.9% BO atoms and 64.4% NBO atoms at V_X and 3,000 K (2.3 GPa), as compared with 33% BO and 67% NBO in enstatite. The remaining 12.5% of O atoms in the liquid are not bound to any Si atoms but rather to Mg atoms, and as such, they are referred to as non-polyhedral oxygen (NPO) or simply as free oxygen. The hydrous phase has more free oxygen, more NBO and fewer BO reflecting the tendency of water to depolymerize the silicate melt. As the liquid is compressed, the proportions of free and NBO decrease whereas those of two and threefold oxygen increase. But the differences between the hydrous and anhydrous melts remain substantial, i.e., the hydrous liquid always remains less polymerized compared to the anhydrous liquid at the same volume. Oxygen triclusters also become abundant at high pressure. A recent experimental study has confirmed the formation of oxygen triclusters in $MgSiO_3$ glass at pressures above 12 GPa (Lee et al. 2008).

To further understand the structural relevance of the Si–O and O–Si coordination, we examine the distribution of the quantity ${}_Z\mathrm{Si}^n$, which is similar to the widely used quantity Q^n defined for fourfold Si–O coordination ($Z = 4$). Here, n is the number of BO (two- or threefold coordinated) attached to a silicon atom, which can be in any coordination state in our case. The calculated distribution consists of a mixture of different species with ${}_Z\mathrm{Si}^1$ and ${}_Z\mathrm{Si}^2$ dominating (37.3 and 37.1% at $V = V_X$ and 3,000 K) at low compression. The ${}_Z\mathrm{Si}^0$ species (10.1%) represents the free-floating polyhedra whereas the ${}_Z\mathrm{Si}^1$ species represents chain-terminating tetrahedra or bi-tetrahedra. Both types of polyhedra are almost absent (less than 0.4%) at the highest compression. As compression increases the distribution becomes wider with gradual increases in the abundances of ${}_Z\mathrm{Si}^4$, ${}_Z\mathrm{Si}^5$ and ${}_Z\mathrm{Si}^6$ species. These three species are present in the amounts of 24.1, 27.0 and 24.9%, respectively, at 77.5 GPa and 3,000 K so almost one third of sixfold coordinated silicon atoms ($Z = 6$) comprise of only BO atoms whereas the remaining silicon atoms also have one or more NBO atoms. The preponderance of higher order species in compressed liquids is consistent with the increased ${}_2C_{OSi}$ and ${}_3C_{OSi}$ values—all indicating an approach to a more ionic, less directional structure on compression.

How the high coordination species are formed from the low coordination species (for example, the appearance of fivefold defects in an otherwise tetrahedral environment) is expected to give useful insight into compression mechanisms and diffusion pathways. Analysis of atomic trajectories reveals three relevant reactions (see Supplementary Figs. 4, 5, 6). First, since melt contains a significant number of free oxygen (not coordinated with any silicon atom), they can contribute to coordination increase: an NPO enters into the coordination shell of the silicon atom thereby increasing the coordination number (Z) but without affecting the number of BOs (n):

$$\mathrm{NPO} + {}_Z\mathrm{Si}^n \rightarrow \mathrm{NBO} + {}_{Z+1}\mathrm{Si}^n, \tag{9}$$

so both the mean Si–O and O–Si coordination increase. Second, NBO atoms can contribute to coordination increase as previously suggested based on experimental studies of sodium silicates (Wolf et al. 1990; Xue et al. 1991; Farber and Williams 1996): an NBO bonded to a neighboring silicon atom becomes bonded to the silicon atom under consideration. This increases the Si–O coordination number as well as the number of BO.

$$\mathrm{NBO} + {}_Z\mathrm{Si}^n \rightarrow \mathrm{BO} + {}_{Z+1}\mathrm{Si}^{n+1}, \tag{10}$$

The two polyhedra share a corner but not necessarily an edge or a face unless they are already sharing another corner or edge. Thus, the overall effect is an exchange of oxygen atoms surrounding a silicon atom via a transitional fivefold coordination state. Our results show that with

increasing pressure the number of NPO decreases only slightly but the numbers of NBO and BO see, respectively, large decrease and increase (Fig. 5, right), so that the reaction (Eq. 10) dominates the pressure-induced coordination increase. Also increased on compression is the threefold O–Si coordination (Fig. 5, right). This requires a third mechanism in which a BO is added to the coordination shell of the Si atom under consideration (Wolf et al. 1990):

$$\mathrm{BO} + {}_{Z}\mathrm{Si}^{n} \rightarrow {}_{3}\mathrm{O} + {}_{Z+1}\mathrm{Si}^{n+1} \qquad (11)$$

The Si atom now has a newly attached O atom, which also bridges other two Si atoms so both Z and n increase.

H and O coordination species

Changes in O–H coordination show a change from dominantly molecular species at low pressure to more extended structures at high pressure. (Fig. 6). As the liquid is compressed, ${}_{1}C_{\mathrm{HO}}$ (onefold H–O coordination) decreases rapidly whereas ${}_{2}C_{\mathrm{HO}}$ (twofold H–O coordination) increases rapidly. Also, ${}_{3}C_{\mathrm{HO}}$ becomes significant at compressed volumes (${}_{0}C_{\mathrm{HO}}$ is negligible at all compression). On the other hand, ${}_{0}C_{\mathrm{OH}}$ is large and decreases with increasing pressure: not all oxygen atoms are bonded with hydrogen and oxygen increasingly participates in O–H bonds on compression. This enhanced participation also results in a gradual increase of the ${}_{1}C_{\mathrm{OH}}$ and ${}_{2}C_{\mathrm{OH}}$ species on compression. Even threefold coordination species becomes significant at high pressures. We find that at low compression more than 50% of H atoms are not coordinated with any other hydrogen so that H–H correlation is significant only at the level of individual structural units. Two types of H–H correlation exist: pairs in which both H atoms are bonded to the same O atom, e.g., water-like groups, and pairs in which two H atoms are bonded to two different O atoms belonging to the same speciation or different speciation. At high compression, more than 50% hydrogen forms two- and threefold coordination even with the appearances of four- and fivefold coordination. Refer Supplementary Fig. 7 for the visualization snapshots of coordination.

Water speciation

V_X and 3,000 K (at 2.3 GPa)

Two types of hydroxyls appear in our simulations (Fig. 7). A polyhedral hydroxyl (PO-H) involves bonding between hydrogen and polyhedral oxygen. The NBO sites are heavily preferred over the BO sites, consistent with the reaction (Stolper 1982): $\mathrm{Si–O–Si} + \mathrm{H_2O} = 2\mathrm{Si–OH}$. In lower abundance (30%) are non-polyhedral (free) hydroxyls (NPO-H), which are bound to only magnesium atoms. Water molecules may also be polyhedral or non-polyhedral (free). Our results show that almost all (~95%) water molecules are non-polyhedral (i.e., bound to Mg atoms). Finally, singly coordinated hydrogen also exists at the ends of extended structures (e.g., H–O–H–O or H–O–H–O–H). H surrounded by two oxygen's (${}_{2}C_{\mathrm{HO}}$) includes polyhedral bridges (Si–O–H–O–Si sequence) and, much less abundantly, edge decoration in which the H is bonded to two oxygens of the same Si–O polyhedron. Edge decoration is not as favorable because the O–O distances along Si–O polyhedral edges (2.685 Å) is more than twice the most probable H–O distance (1.005 Å).

We calculate abundances of different forms of water speciation as a function of pressure at different temperatures (Table 2, Fig. 8). By using the calculated concentrations of hydroxyls, water molecules and free oxygen (not bonded to hydrogen), we can also estimate the equilibrium constant of the reaction $\mathrm{O} + \mathrm{H_2O} \leftrightarrow 2\mathrm{OH}$ as $9.30^2/(27.83 \times 0.96) = 3.23$ at V_X (2.3 GPa) and 3,000 K. Here, the numbers of hydroxyls (9.30) and water molecules (0.96) were derived from their values (58.13 and 11.96% hydrogen, respectively) in Table 2, and the number of free oxygens (27.83) was derived from its value (63.25% oxygen) in Table 2. Similarly, the equilibrium constant value at 2,000 K is $8.58^2/(28.39 \times 1.49) = 1.74$. They are comparable with the value (2.3) extrapolated from

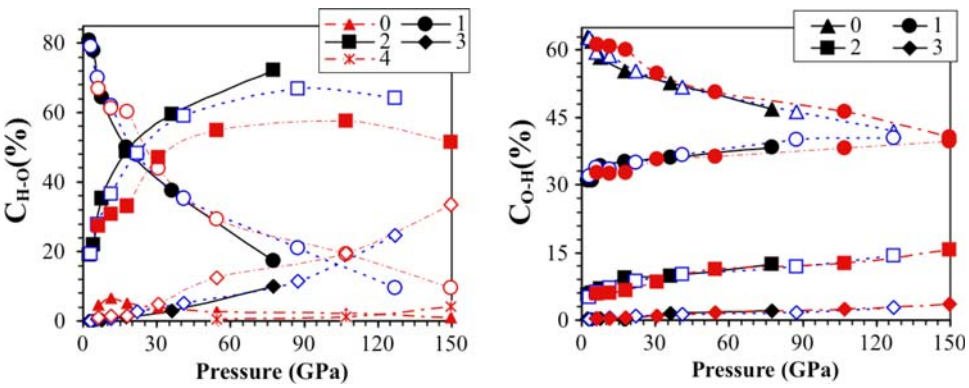

Fig. 6 Abundances of different species of H–O and O–H coordination as a function of pressure at 3,000 K (*black solid lines* and *black symbols*), 4,000 K (*blue dotted lines* and *blue symbols*) and 6,000 K (*red dashed-dotted lines* and *red symbols*) for the hydrous melt

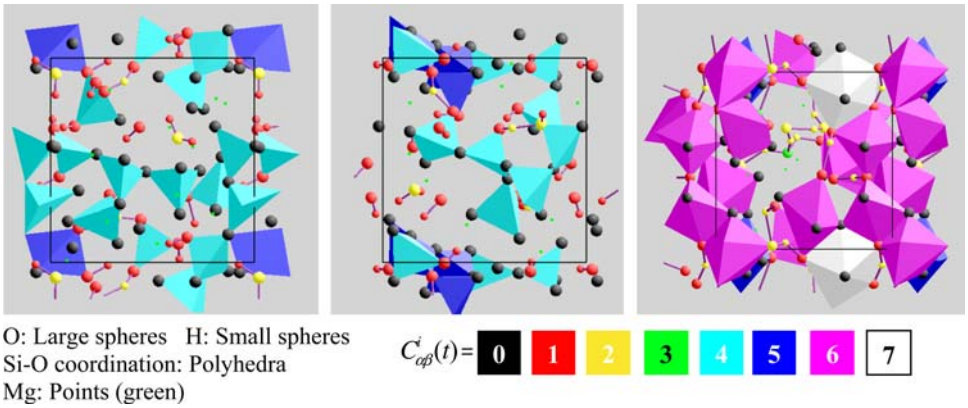

Fig. 7 Snapshots of water speciation in relation with H and O coordination at V_X and 3,000 K (*left* and *center*) and 0.5 V_X and 3,000 K (*right*). Color encodes coordination: *black* (zerofold) to *white* (sevenfold). The sequences of *small* (hydrogen) and *big* (oxygen) *spheres* in *red*, *yellow* and *green* (representing one-, two- and threefold coordination, respectively) colors visually represent different species. A hydroxyl appears as a *big red sphere–small red sphere* pair (simply a *red–red* pair). Similarly, a water molecule appears as a *small red sphere–big yellow sphere–small red sphere* triplet whereas a bridging structure appears as a *big red sphere–small yellow sphere–large red sphere* triplet. In any polyhedral association, O appears as a sphere at a polyhedral corner otherwise it appears as a free sphere (attached to an Mg atom). Edge decoration, four-atom sequences, and long sequences containing threefold coordinated O and H atoms are also present

Table 2 Abundances (in the percentage of total hydrogen number, which is 16) of different forms of water speciation in the hydrous melt (10 wt% water) at different conditions

Species	V_X, 2,000 K 1.1 GPa	V_X, 3,000 K 2.3 GPa	V_X, 3,000 K (GGA)	V_X, 3,000 K (5 wt%)	0.5 V_X, 3,000 K 77.5 GPa	0.45 V_X, 4,000 K 127.1 GPa	0.45 V_X, 6,000 K 149.8 GPa
Free H	0.00	0.05	0.08	0.01	0.00	0.02	0.34
Hydroxyl	53.62	58.13	61.81	68.58	7.54	3.42	2.48
Water	18.58	11.96	13.99	4.11	0.09	0.04	0.13
Bridging	8.21	8.00	6.97	15.80	20.16	14.36	9.83
2O2H	10.48	11.88	9.61	8.03	4.56	1.28	1.10
H3O	0.00	0.01	0.00	0.04	1.59	3.04	3.86
Hydronium	0.03	0.11	0.08	0.17	0.00	0.00	0.00
3O2H	1.17	1.32	1.25	1.84	10.71	7.1	4.60
2O3H	3.65	3.43	2.96	0.63	0.93	0.02	1.10
Others	4.26	5.11	3.25	0.79	54.42	70.72	76.56
Free O	35.48	36.75	36.98	20.35	53.05	58.07	60.02

The last row shows the amount of free oxygen (which does not participate in hydrogen bonding) in the percentage of total oxygen number, which is 44. Also shown are the results for low water content (5 wt%) at V_X (1.6 GPa) and 3,000 K (for which the total numbers of H and O atoms are 8 and 46, respectively)

experimental measurements on rhyolite compositions (Zhang 1999) at much lower temperatures and water contents.

0.5 V_X and 3,000 K (at 77.5 GPa)

Water speciation at high pressure is entirely different, with molecular species being replaced by extended structures (Fig. 7). Hydroxyls and water molecules are rare, with most ${}_1C_{HO}$ arising from chain terminations (…–O–H–O–H). Twofold H–O coordination results from dramatically enhanced amounts of bridging (X–O–H–O–X, with X = Mg, Si), and polyhedral edge decoration. The latter form of high pressure H incorporation was suggested by Closmann and Williams (1995). Threefold H–O coordination is also significant in which the same H atom forms a mixture of bridging and edge decoration. A face decoration in which H atom is coordinated with three O atoms defining a polyhedral face (i.e., a pure three-way edge decoration) was not seen. The O–H coordination number shows that more than half of the O atoms are involved in the water speciation at high compression. The greater

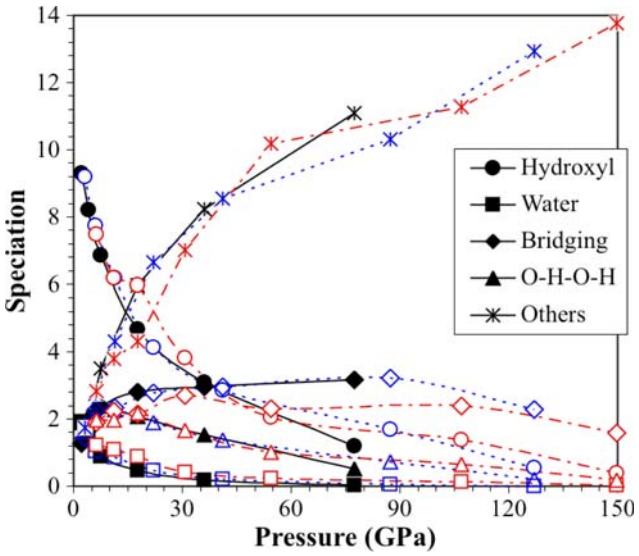

Fig. 8 Abundances (expressed in terms of the number of hydrogen atoms) of different types of water speciation as a function of pressure at 3,000 K (*black solid lines* and *black symbols*), 4,000 K (*blue dashed lines* and *blue symbols*) and 6,000 K (*red dashed-dotted lines* and *red symbols*). Note that the total number of hydrogen atoms in the melt is 16

participation of O in O–H bonding is consistent with our finding that the solubility of water in the silicate melt is unlimited at high pressure and that the silicate–water system becomes increasingly ideal on compression. The extended structures can extend across the entire supercell. Figure 7 (right) shows a 14-atom structure, which comprises of 7 H atoms and 7 O atoms running from the near mid left boundary toward the upper right corner. Note that branching occurs at threefold coordinated O atom. The total abundance of extended structures (those containing threefold coordinated atoms and/or five or more atoms) increases monotonically with increasing pressure (Fig. 8). Most contributions come from the structures consisting of more than five atoms (54.4 and 76.6%, respectively, at 77.5 and 149.8 GPa).

Water content

To investigate the dependence of water speciation on water content, we have simulated silicate liquid containing a smaller amount of water (5 wt%) at V_X (1.6 GPa) and 3,000 K (Tables 1, 2). There are more hydroxyl groups ($\sim$69%) and less molecular water ($\sim$4%) in the low water content liquid, compared to the high content case. The proportion of isolated bridging (X–O–H–O–X, where X = Mg or Si) is slightly enhanced whereas all bigger structures (containing four or more atoms) are suppressed with decreasing water content. Our prediction that water dissolves increasingly as molecular water as the total water content of the silicate melt increases is qualitatively consistent with experimental observations (Stolper 1982). As expected diminished water content leads to diminished depolymerization, with values of the O–Si coordination number falling in between those of the anhydrous and 10 wt% water structures (Table 1).

Dynamical properties: results and discussion

Diffusion coefficients

The calculated partial diffusion coefficients (using Eq. 8) as a function of pressure and temperature (Fig. 9) are shown to follow the Arrhenius relation with fit parameters (Table 3). Our results are consistent with the experimental values for hydrogen (Zhang and Stolper 1991), and silicon and oxygen (Lesher et al. 1996; Tinker et al. 2003) diffusion in basaltic melts. The differences may be partly due to relatively low temperatures (below 2,000 K) of experiments and partly due to compositional differences. Hydrogen diffusivity differences from the previous results (Mookherjee et al. 2008) are within computational uncertainties, and are due to longer runs used in this study. We find that water enhances the diffusivity of all species (Fig. 9). The calculated diffusivities for low water content melt are slightly lower than those for high water content melt. Also, the proton diffusivity is weakly sensitive to the water content. The hydrogen diffusivity is much higher than the diffusivities of other species at all conditions. The framework silicon ions are the slowest moving species and tend to show diffusivity increasing with pressure initially, reaching a maximum value, before decreasing on further compression. Such pressure-induced diffusion maxima were previously predicted in anhydrous $MgSiO_3$ liquid (Kubicki and Lasaga 1991; Wasserman et al. 1993) and found to be more pronounced in SiO_2 (Karki et al. 2007) and silica-rich (e.g., Lacks et al. 2007) liquids.

To explore the atomic-scale mechanisms of diffusion, we quantify H–O, Mg–O and Si–O bond lifetimes (Fig. 10 and Supplementary Fig. 8). Most H–O bonds have lifetimes less than 50 fs; we were able to measure bonds with lifetimes as long as 5,000 fs. The bond lifetime histogram shows a nearly power-law fall-off in the number of bonds with increasing lifetime. The effects of compression on bond lifetimes are shown to be substantial. Although the H–O bonds of short lifetimes become more abundant on compression, relatively long-lived H–O bonds (with lifetimes of 500 fs or longer) are more abundant at low compression (Fig. 10). Also, such long-lived bonds become more abundant at lower temperature. This is consistent with preponderance of hydroxyls and molecular water at low compression. We also determine the rate of

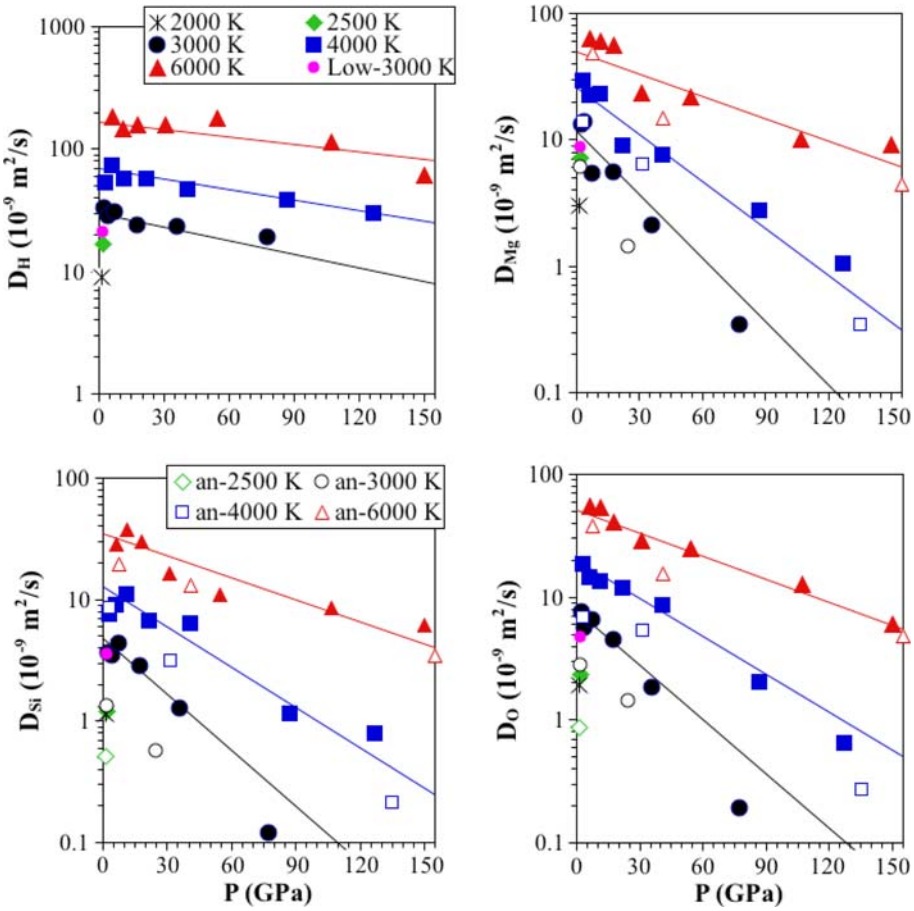

Fig. 9 Diffusivities for H, Mg, Si and O in the hydrous melt as a function of pressure at 3,000 K (*circles*), 4,000 K (*squares*) and 6,000 K (*triangles*). *Open symbols* are the corresponding results for anhydrous melt. The *lines* are Arrhenius fits to the hydrous data. Also shown are the results at 2,000 K (*asterisk*, only for hydrous melt) and 2,500 K (*diamonds*) at V_X. The results for the low (5 wt%) water content at 3,000 K and V_X are shown by small circles

Table 3 Activation energies and volumes of diffusion for different species derived from Arrhenius fit: $D = D_0\exp[-(E_A + PV_A)/RT]$

Parameters	H	Mg	Si	O
D_0 ($\times 10^{-9}$ m^2/s)	920	280	250	240
E_A (kJ/mol)	85	79	97	94
MD		77	102	91
Expt	128[a]		176[b]–229[c]	180[c]–211[c]
V_A (Å^3)	0.27	1.75	1.35	1.32

The previous MD results are for anhydrous enstatite liquid from Kubicki and Lasaga (1991). The experimental data are for hydrous (Zhang and Stolper 1991)[a] and anhydrous (Lesher et al. 1996[b] and Tinker et al. 2003[c]) basaltic melts

bond-breaking events, α_B (Table 4). Both compression and temperature enhance the bond-breaking rates. However, not all events contribute to hydrogen diffusion since there are two processes involved: First is hydrogen recombination in which a given H–O bond is broken momentarily and then formed again so a new bond is not formed. Second is hydrogen transfer in which one H–O bond is broken and a different H–O bond is formed. As a result, the hydrogen atom gets transferred from one oxygen atom to another oxygen atom. Since free H atoms are extremely rare, the rupture of the first bond cannot occur before the formation of a new bond indicating the importance of intermediate state in hydrogen transfer. One can estimate the proportion of hydrogen transfers by counting the number of distinct H–O bonds that exist during a finite time period. Let N_B be such number for a period of 1 ps. We can define the ratio of the transfers to the bond-breaking events as $(N_B - n_B)/\alpha_B$, where n_B is the average number of H–O bonds per step (=16 × mean coordination number). Smaller ratios at higher compression and lower temperatures are consistent with the smaller values of hydrogen diffusivity at those conditions (Table 4).

Hydrogen diffusion mechanisms

We analyze MD snapshots in order to further explore the mechanisms of hydrogen diffusion. Two modes of H diffusion are of interest. One mode involves the movement of H atoms through the rupture and formation of O–H bonds whereas the other mode involves the movement of hydroxyls or water molecules through the rupture and formation of Si–O and Mg–O bonds. Since the numbers of free H atoms (i.e., not bonded to any O) and free O atoms (i.e., not bonded to any cation) are nearly 0, all hydrogen

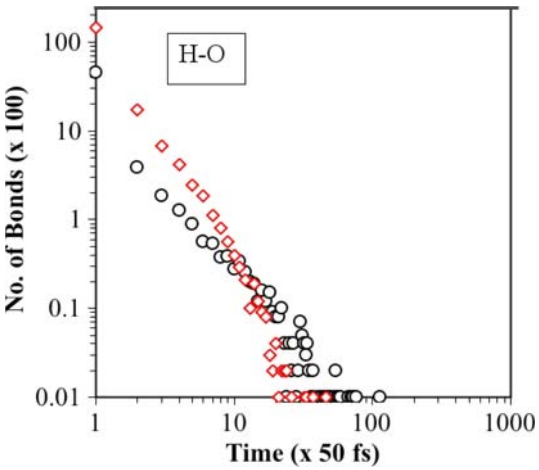

Fig. 10 Distributions of H–O bond lifetimes at V_X, 3,000 K (*circles*) and 0.5 V_X, 3,000 K (*diamonds*) for the hydrous melt

must be attached to the Si–Mg matrix in the form of Si–O–H groups or Mg–O–H groups or in the mixed forms. During diffusion, an H atom is transferred from one group to another group. Several combinations of the source and destination groups for the H transfer are possible.

We first consider the cases where both the source and destination groups involve polyhedral oxygen (PO), which can be NBO or BO. The simplest but perhaps the most common case is

$$\mathrm{PO{-}H\cdots PO} \rightarrow \mathrm{PO{-}H{-}PO} \rightarrow \mathrm{PO\cdots H{-}PO} \qquad (12)$$

Here, the H atom moves from one PO to another PO thereby breaking the bond with the first oxygen and forming a new bond with the second oxygen. Figure 11 (top) illustrates the transfer of an H atom from one polyhedral O to another polyhedral O via a momentary formation of H bridging. The high abundance of hydroxyls and bridging support this mechanism. While polyhedral bridging is strongly favored, if both the source and destination O atoms belong to the same polyhedron, the H atom simply decorates an edge in the intermediate state. In the general form of the above reaction, the source may contain one or more H atoms (i.e., it may be a polyhedral hydroxyl or a polyhedral water or a part of some extended structure) and the destination may also contain zero or more H atoms (i.e., may be a PO or a polyhedral hydroxyl or even a polyhedral water or a part of some extended structure). A hydronium can serve only as an intermediate state because of its relative short lifetime and low abundance.

An H atom bound to PO can be released to NPO (Fig. 11, bottom). Since NPO is always involved in H-bonding, it must be already bonded to, at least, one H atom. In the simplest (but the most common) case, the reactants are the source polyhedral hydroxyl (preferably, NBO–H) and the destination non-polyhedral hydroxyl.

$$\begin{aligned}\mathrm{PO{-}H\cdots NPO{-}H} &\rightarrow \mathrm{PO{-}H{-}NPO{-}H} \\ &\rightarrow \mathrm{PO\cdots H{-}NPO{-}H}\end{aligned} \qquad (13)$$

The intermediate stage must involve water-like group (about Mg atom), with one H shared between PO and NPO, and other H attached only to NPO. This four-atom structure is quite abundant at low compression. The PO-H bond eventually breaks thereby forming an Mg-bound water molecule (H–NPO-H). This reaction may be subsequently followed by another reaction in which the newly formed water molecules loses one H atom to a different PO (see Supplementary Fig. 9). Unlike above two transfers, in the case of NPO to NPO transfer, the source O atom must have already, at least, two H atoms attached (i.e., water-like group) whereas the destination O must have, at least, one H atom so a minimum of three H atoms are involved. The number of NPO is relatively small at all pressures so finding two NPOs sufficiently close to each other is less likely.

We now explore the mechanism in which stable hydroxyls and water molecules serve as hydrogen carriers (Supplementary Fig. 10). Since NPO atoms are always bonded to one or more H atoms and some O–H bonds are stable for extended durations, the motion of such units can proceed through the rupture and formation of Mg–O and/or Si–O bonds without breaking H–O bond. Diffusion in the form of hydroxyl can be described by:

$$\mathrm{X{-}OH\cdots Y} \rightarrow \mathrm{X{-}OH{-}Y} \rightarrow \mathrm{X\cdots HO{-}Y}, \qquad (14)$$

Table 4 Various H–O bond related parameters (α_B = rate of bond-breaking events, n_B = average number of H–O bonds per step, N_B = number of distinct H–O bonds) and hydrogen diffusivity (D_H) at different conditions

V, T (K), P (GPa)	α_B (Events/ps)	n_B	N_B (during 1 ps)	$(N_B - n_B)/\alpha_B$	D_H ($\times 10^{-9}$ m^2/s)
V_X, 2,000, 1.1	179	18.7	77	0.32	8.9
V_X, 3,000, 2.3	234	18.7	106	0.37	33.1
V_X, 4,000, 3.3	288	18.9	161	0.49	52.9
0.7 V_X, 3,000, 17.6	456	24.2	170	0.32	24.0
0.5 V_X, 3,000, 77.5	723	30.6	195	0.23	18.9
0.45 V_X, 4,000, 127.1	2180	34.2	420	0.18	30.4
0.45 V_X, 6,000, 149.8	1532	36.9	438	0.26	61.2

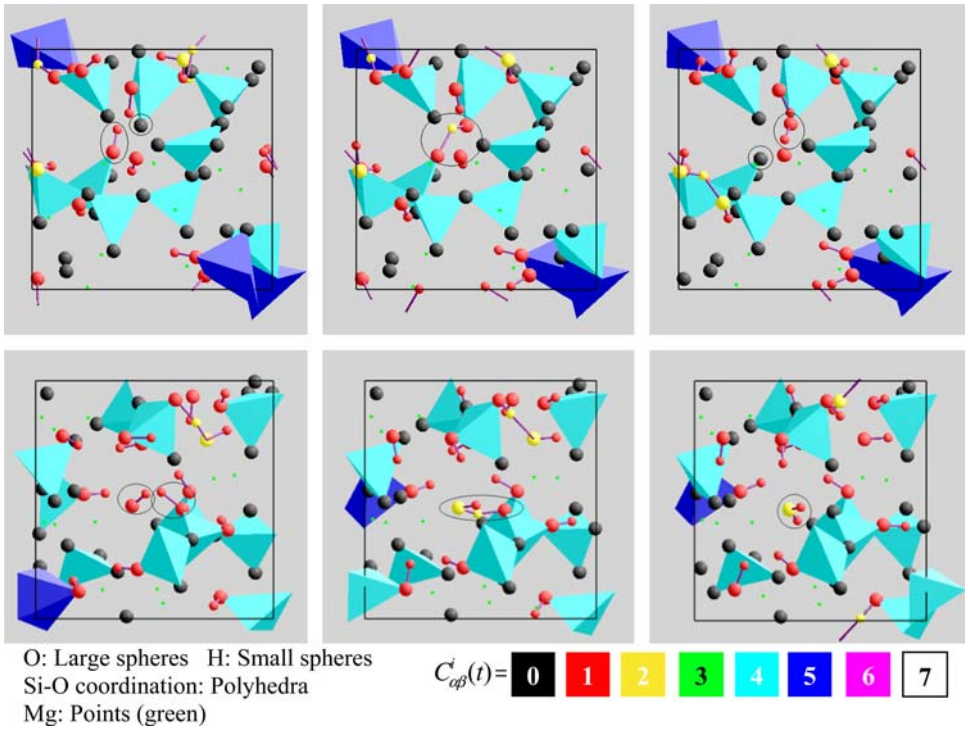

Fig. 11 *Top*: The initial (*left*), intermediate (*center*) and final (*right*), of the H transfer between two non-bridging oxygen atoms marked by circles. *Bottom*: Stages of the H transfer from PO to NPO marked by *circles*. Color encodes coordination: *black* (zerofold) to *white* (sevenfold)

where X, Y = Si or Mg. We assume that the H–O bond remains stable during its transfer from one cation (X) to another (Y). Such transfer is more common during time periods when the O atom is not a part of any polyhedron for two reasons: First, a non-polyhedral hydroxyl does not disintegrate until it is turned into a non-polyhedral water or water-like group or a polyhedral hydroxyl. Second, Mg–O bonds have much shorter lifetimes than Si–O bonds. The above reactions also hold for the case of water molecule considered as a moving species but water molecules (free) are much less abundant than hydroxyls and are almost absent at high compression. Also, non-polyhedral water can loose one H atom at any time. The direct H transfer mechanism involving PO and NPO can be considered occurring together with hydroxyl/water transfer mechanism (see Supplementary Description 1).

Finally, an interesting point to note is that the diffusion coefficient of hydrogen decreases on compression not as much as the diffusion coefficients of other atoms do (Fig. 9). The hydrogen diffusivity deceases only by a factor of about two from V_X to 0.45 V_X whereas the other atom diffusivities decrease by a factor of about ten over the same compression regime. In the context of the Arrhenius relation, this is attributed to a smaller activation volume for H as compared with the other ions. The large contrast in the pressure variation of the diffusivity between hydrogen and other species can better be understood in terms of hydrogen diffusion mechanisms, which change with compression. At low compression, the diffusion occurs in the form of H atoms as well as hydroxyls (to some extent, also water molecules). Hydroxyls and water molecules are slow moving carriers compared to H atoms. However, the presence of hydroxyls and water molecules is strongly suppressed with compression so it is individual proton transfer that essentially controls the diffusivity at high pressure. In other words, slow moving species are not present in large amounts so as to lower the diffusivity that would be otherwise due to highly mobile protons at high pressure to the same extent as they do at low pressure.

Acknowledgments This work is supported by National Science Foundation (EAR-0809489). The authors thank Center of Computation and Technology (CCT) at Louisiana State University for computing resources.

References

Angell CA, Cheeseman PA, Tamaddon S (1982) Pressure enhancement of ion mobilities in liquid silicates from computer-simulation studies to 800-kilobars. Science 218:885–887

Bercovici D, Karato S (2003) Whole mantle convection and the transition-zone water filter. Nature 425:39–44

Bhattarai D, Karki BB (2009) Atomistic visualization: space–time multiresolution integration of data analysis and rendering. J Mol Graph Model 27:951–968

Ceperley DM, Alder BJ (1980) Ground state of the electron gas by a stochastic method. Phys Rev Lett 45:566–569

Closmann C, Williams Q (1995) In-situ spectroscopic investigation of high-pressure hydrated (Mg, Fe)SiO3 glasses—OH vibrations as a probe of glass structure. Am Mineral 80:201–212

de Koker N, Stixrude L, Karki BB (2008) Thermodynamics, structure, dynamics, and melting of Mg_2SiO_4 liquid at high pressure. Geochim Cosmochim Acta 72:1427–1441

Farber DL, Williams Q (1996) An in situ Raman spectroscopic study of $Na_2Si_2O_5$ at high pressures and temperatures: structure of compressed liquids and glasses. Am Mineral 81:273–283

Funamori N, Yamamoto S, Yagi T, Kikegawa T (2004) Exploratory studies of silicate melt structure at high pressures and temperatures by in situ X-ray diffraction. J Geophys Res 109:B03203

Giordano D, Romano DB, Dingwell DB, Poe B, Behrens H (2004) The combined effects of water and fluorine on the viscosity of silicic magmas. Geochim Cosmochim Acta 68:5159

Goldman N, Fried LE, Kuo IFW, Mundy CJ (2005) Bonding in the superionic phase of water. Phys Rev Lett 94:217801

Goncharov AF, Struzhkin VV, Mao HK, Hemley RJ (1999) Raman spectroscopy of dense H_2O and the transition to symmetric hydrogen bonds. Phys Rev Lett 83:1998–2001

Inoue T (1994) Effect of water on melting phase relations and melt composition in the system Mg_2SiO_4–$MgSiO_3$–H_2O up to 15 GPa. Phys Earth Planet Inter 85:237–263

Karki BB, Bhattarai D, Stixrude L (2007) First principles simulations of liquid silica: structural and dynamical behavior at high pressure. Phys Rev B 76:104205

Kresse G, Furthmuller J (1996) Efficiency of ab-initio total energy calculations for metals and semiconductors using a plane-wave basis set. Comput Mater Sci 6:15–50

Kresse G, Hafner J (1994) Norm-conserving and ultrasoft pseudopotentials for first-row and transition-elements. J Phys Condens Matter 6:8245–8257

Kubicki JD, Lasaga AC (1991) Molecular dynamics simulations of pressure and temperature effects on $MgSiO_3$ and Mg_2SiO_4 melts and glasses. Phys Chem Miner 17:661–673

Lacks DJ, Rear DB, Van Orman JA (2007) Molecular dynamics investigation of viscosity, chemical diffusivities and partial molar volumes of liquids along the MgO–SiO_2 joins as functions of pressure. Geochim Cosmochim Acta 71:1312–1323

Lange RA (1994) The effect of H_2O, CO_2 and F on the density and viscosity of silicate melts. Rev Mineral 30:331–369

Lange RA, Carmichael ISE (1987) Densities of Na_2O–K_2O–MgO–FeO–Fe_2O_3–Al_2O_3–TiO_2–SiO_2 liquids—new measurements and derived partial molar properties. Geochim Cosmochim Acta 51:2931–2946

Lee SK, Li JF, Cai YQ, Hiraoka N, Eng PJ, Okuchi T, Mao HK, Meng Y, Hu MY, Chow P, Shu J, Li B, Fukui H, Lee BH, Kim HN, Yoo CS (2008) X-ray Raman scattering study of $MgSiO_3$ glass at high pressure: implication for triclustered $MgSiO_3$ melt in Earth's mantle. Proc Natl Acad Sci USA 105:7925–7929

Lesher CE, Hervig RL, Tinker D (1996) Self diffusion of network formers (silicon and oxygen) in naturally occurring basaltic liquid. Geochim Cosmochim Acta 60:405–413

Mao WL, Mao HK, Meng Y, Eng PJ, Hu MY, Chow P, Cai YQ, Shu J, Hemley RJ (2006) X-ray-induced dissociation of H_2O and formation of O_2–H_2 alloy at high pressure. Science 314:636–638

Martin GB, Spera FJ, Ghiorso MS, Nevins D (2009) Structure, thermodynamic and transport properties of molten Mg_2SiO_4: molecular dynamics simulations and model EOS. Am Mineral 94:693–703

Matsukage K, Zhicheng J, Karato S (2005) Density of hydrous silicate melt at the conditions of Earth's deep mantle. Nature 438:488–491

Mermin ND (1965) Thermal properties of inhomogeneous electron gas. Phys Rev 137:A1441–A1443

Mookherjee M, Stixrude L, Karki BB (2008) Hydrous silicate melt at high pressure. Nature 452:983–986

Ochs FA, Lange RA (1999) The density of hydrous magmatic liquids. Science 283:1314–1317

Pohlmann M, Benoit M, Kob W (2004) First-principles molecular dynamics simulations of a hydrous silica melt: structural properties and hydrogen diffusion mechanism. Phys Rev B 70:184209

Revenaugh J, Sipkin SA (1994) Seismic evidence for silicate melt atop the 410-km mantle discontinuity. Nature 369:474–476

Rustad JR, Yuen DA, Spera FJ (1990) Molecular-dynamics of liquid SiO_2 under high-pressure. Phys Rev A 42:2081–2089

Sakamaki T, Suzuki A, Ohtani E (2006) Stability of hydrous melt at the base of the Earth's upper mantle. Nature 439:192–194

Shen A, Keppler H (1995) Infrared spectroscopy of hydrous silicate melts to 1000°C and 10 kbar: direct observation of H_2O speciation in a diamond-anvil cell. Am Mineral 80:1335–1338

Shen A, Keppler H (1997) Direct observation of complete miscibility the albite-H_2O system. Nature 385:710–712

Stixrude L, Karki BB (2005) Structure and freezing of $MgSiO_3$ liquid in Earth's lower mantle. Science 310:297–299

Stixrude L, Lithgow-Bertelloni C (2005) Thermodynamics of mantle minerals. I. Physical properties. Geophys J Int 162:610–632

Stolper EM (1982) The speciation of water in silicate melts. Geochim Cosmochim Acta 46:2609–2620

Tinker D, Lesher CE, Hutcheon (2003) Self-diffusion of Si and O in diopside–anorthite melt at high pressure. Geochim Cosmochim Acta 67:133–142

Tsuneyuki S, Matsui Y (1995) Molecular dynamics study of pressure enhancement of ion mobilities in liquid silica. Phys Rev Lett 74:3197–3200

Tyburczy JA, Duffy TS, Ahrens TJ, Lange MA (1991) Shock wave equation of state of serpentine to 150 GPa: implications for the occurrence of water in the Earth's mantle. J Geophys Res 96:18011–18027

Wan TK, Duffy TS, Scandolo S, Car R (2007) First principles study of density, viscosity and diffusion coefficients of liquid $MgSiO_3$ at conditions of the Earth's deep mantle. J Geophys Res 112:03208. doi:10.1029/2005JB004135

Wang Y, Perdew J (1991) Correlation hole of the spin-polarized electron gas with exact small-wave-vector and high-density scaling. Phys Rev B 44:13298–13307

Waseda Y, Toguri JM (1990) Structure of silicate melts determined by X-ray diffraction. In: Marumo F (ed) Dynamics process of material transport and transformation in earth's interior. Terra Scientific Publishing Company, Tokyo, pp 37–51

Wasserman EA, Yuen DA, Rustad JR (1993) Molecular dynamics study of the transport properties of perovskite melts under high temperature and pressure conditions. Earth Planet Sci Lett 114:373–384

Watson EB (1981) Diffusion in magmas at depth in the Earth: the effects of pressure and dissolved H_2O. Earth Planet Sci Lett 52:291–301

Wentzcovitch RM, Martins JL, Allen PB (1992) Energy versus free-energy conservation in first-principles molecular dynamics. Phys Rev B 45:11372–11374

Whittington A, Richet P, Holtz F (2000) Water and the viscosity of depolymerized aluminosilicate melts. Geochim Cosmochim Acta 64:3725

Williams Q, Jeanloz R (1988) Spectroscopic evidence for pressure-induced coordination changes in silicate-glasses and melts. Science 239:902–905

Wolf GH, Durben DJ, McMillan PF (1990) High-pressure Raman spectroscopic study of sodium tetrasilicate ($Na_2Si_4O_9$) galls. J Chem Phys 93:2280–2288

Xue X, Stebbins JF, Kanzaki M, McMillan PF, Poe B (1991) Pressure induced silicon coordination and tetrahedral structural changes in alkali silicate melts up to 12 GPa: NMR, Raman, and infrared spectroscopy. Am Mineral 76:8–26

Yamada Y, Inoue T, Irifune T (2004) Melting of enstatite from 13 to 18 GPa under hydrous conditions. Phys Earth Planet Inter 147:45–56

Yamada A, Inoue T, Urakawa A, Funakoshi K, Funamori N, Kikegawa T, Ohfuji H, Irifune T (2007) In situ X-ray experiment on the structure of hydrous Mg–Silicate melt under high pressure and high temperature. Geophys Res Lett 34:L10303

Zhang Y (1999) H_2O in rhyolitic glasses and melts: measurement, speciation, solubility and diffusion. Rev Geophys 37:493–516

Zhang Y, Stolper EM (1991) Water diffusion in a basaltic melt. Nature 351:306–309

Zhang G, Guo G, Refson K, Zhao Y (2004) Finite-size effects at both high and low temperatures in molecular dynamics calculations of the self-diffusion coefficient and viscosity of liquid silica. J Phys Condens Matter 16:9127–9135

Zhang Y, Xu Z, Zhu M, Wang H (2007) Silicate melt properties and volcanic eruptions. Rev Geophys 45:RG4004. doi:10.1029/2006RG000216